Role of the ligand density in cation exchange materials for the purification of proteins

Agnes Franke[a], Nicola Forrer[a], Alessandro Butté[b], Božidar Cvijetić[a], Massimo Morbidelli[a,*], Matthias Jöhnck[c], Michael Schulte[c]

[a] Institute for Chemical and Bioengineering, Department of Chemistry and Applied Biosciences, ETH Zurich, Wolfgang Pauli Strasse, 8093 Zurich, Switzerland
[b] LES R & D - DSP Technologies, Lonza AG, 3930 Visp, Switzerland
[c] Merck KGaA, Life Science Solutions Performance & Life Science Chemicals, Frankfurter Str. 250, 64293 Darmstadt, Germany

ARTICLE INFO

ABSTRACT

The performance of functionalized materials, such as cation exchange resins, is dependent not only on the ligand type and ligand density, but also on the pore accessibility of the target molecule. In the case of large molecules such as antibodies this latter parameter becomes crucial, because the size of such molecules falls somewhere inside the pore size distribution of the resin. The influence of the ligand density and accessibility on the overall performance of the material is explored systematically. Five different materials, having the same chemistry as the strong cation exchange resin Fractogel EMD SO_3^- (M) , have been analyzed. These materials only differ in the ligand density. It is shown that the ligand density directly influences the porosity of the materials as well as the pore diffusivity and the dynamic binding capacity. For a given purification problem an optimal ligand density can be found. Based on the above results a new material is proposed, showing superior properties in terms of dynamic binding capacity. This is achieved by an optimization of the ligand density and by a decrease of the particle size of the stationary phase. The material properties are modeled with a general rate model. Further simulations were conducted to evaluate the performance of the new material in comparison with a conventional resin.

1. Introduction

Within the pharmaceutical industry, the production of monoclonal antibodies is the fastest growing sector [1]. For 2009, an annual production of 14 t of monoclonal antibodies is forecasted [2]. The upstream process made great progress within the last couple of years, so that it is possible to reach antibody titers as high as 10 g/l. As a result, the downstream process arrived to account for 50–80% of the production costs [3]. The classical approach for the purification of immunoglobulin G (IgG) typically starts with a capture step by Protein A affinity chromatography followed by a number of chromatographic and non-chromatographic steps [4]. The main advantage of the affinity step is the extremely high selectivity towards antibodies. The drawback of this method is the high resin price. Furthermore, Protein A is highly toxic [5]. Therefore, the removal of leaking Protein A must be proven in subsequent purification steps. In order to overcome this problem, alternative purification strategies have been proposed [6]. Promising alternatives include ion exchange and hydrophobic interaction materials [7,8]. Furthermore, new stationary phases have been introduced that combine both previously mentioned effects, the so-called mixed mode materials [9–12]. In this regard, ion exchange resins appear particulary promising due to their comparably low cost and their ability to both capture and resolve different proteins [13].

Many authors evaluated and compared stationary phases in order to find the best material for a given separation problem. Staby et al. [14–19] measured the properties of anion as well as cation exchange resins extensively. Ghose et al. [20] compared the properties of hydrophobic charge induction materials to Protein A mimetic and Protein A resins. Pore size and retention factors of hydrophobic interaction materials were studied for a set of proteins by To and Lenhoff [21]. However, in all cases materials from different suppliers were compared. As differences in the synthesis and manufacturing of the resins might lead to significant differences in the performance for a certain kind of application, a fair comparison of those materials is difficult. In particular, it is hard to link certain performance data directly to a material property, because the information about each material is incomplete.

Historically, ion exchange resins were developed for the purification and analysis of small molecules [22]. Their application to the purification of proteins introduces a manifold of new problems due

to the fact that antibodies such as IgG has dimensions comparable to the pore sizes. This leads not only to high mass transfer resistances, but also to limited accessibility of the protein into the pores of the stationary phase. As it will be discussed in detail in this work, some other factors, such as the particle size and especially the ligand density of the support, play an important role here. The influence of the latter on the performance of ion exchange materials has already been studied by Wu and Walters for silica supports in 1992 [23]. However, they chose rather small proteins such as lysozyme and cytochrome c. Zhang and Sun [24] studied the behavior of bovine serum albumin and bovine hemoglobin on affinity resins with different ligand densities. Langford et al. [25] studied the mass transfer of lysozyme on a set of cation exchange resins with varying ligand density.

In this work, a set of custom made cation exchange resins are studied regarding pore size distribution, ligand density and particle size in order to find the effect of those parameters on mass transfer resistances and static and dynamic binding capacity for IgG. To our knowledge, these parameters have not been analyzed systematically for large biomolecules such as IgG. In the first part of the work, all analyzed materials have the same polymeric support as the commercial material Fractogel EMD SO_3^- (M).

Based on the obtained results, a new cation exchange material, tailor made for the purification of IgG, i.e. FractoAIMs, is developed in the second part of this work. The behavior of this material and the benchmark material Fractogel EMD SO_3^- (M) is simulated with a general rate model. This model considers the concentration distribution of the solutes in the axial direction along the chromatographic column as well as along the radial direction in the stationary phase [26]. Even though the model needs to solve a large number of differential equations, its application is needed in the case of systems with dominating mass transfer resistances [27]. The objective here is to verify the possibility of such a model to predict the dynamic binding capacity of a given stationary phase. This could help tremendously in the screening phase of operating conditions and stationary phases by avoiding the dynamic column breakthrough experiments which require time and materials not always available in the early stage of process development.

The combination of a rational design of a new material, based on experimental data, with the simulation of the behavior of IgG on this material gives new insights in the mode of operation of ion exchange resins for preparative protein purification. Accordingly, this paper provides a new design strategy for preparative stationary phases for the purification of large molecules.

2. Materials and instrumentation

Strong cation exchange resin Fractogel EMD SO_3^- (M), that was chosen as a benchmark material, was provided by Merck (Darmstadt, Germany). It has a crosslinked polymethacrylate matrix with sulfoisobutyl as functional groups. These are bound to the matrix with linear polymer chains, the so-called 'tentacles' [28]. The particle size of Fractogel EMD SO_3^- (M) is $d_p = 40 - 90$ μm (average $d_p = 65$ μm) with a pore size of about $r_p = 400$ Å. For large scale operation, Fractogel EMD SO_3^- (M) is operated at velocities up to $u_{lin} = 350$ cm/h. As the columns used in this work are much shorter, it was possible to flow pack the resin at a velocity of $u_{lin} = 800$ cm/h. The maximum velocity for chromatographic experiments is set to a linear velocity of $u_{lin} = 400$ cm/h.

Based on the same support used for Fractogel EMD SO_3^- (M), Merck (Darmstadt, Germany) synthesized materials with different ligand densities (Series 1, see Table 1). Furthermore, a new material called FractoAIMs, was developed by Merck within this work. This material has an average particle size of 40 μm. It was designed in order to have a high rigidity which leads to a much higher oper-

ating flow rate than Fractogel EMD SO_3^- (M), also at preparative conditions. Therefore, FractoAIMs was flow packed with a velocity of $u_{lin} = 1100$ cm/h in this work. The ligand density of all materials was evaluated by the supplier by titration as summarized in Table 1.

Gammanorm, which is human normal immunoglobulin G (IgG > 95%) in solution ($c_{IgG} = 165$ g/l), has been chosen as an model protein to investigate the behavior of antibodies on ion exchange materials. The polyclonal antibody mixture was purchased at Octapharma (Lachen, Switzerland). Human serum albumin and myoglobin from equine sceletal muscle were purchased at Sigma–Aldrich (Buchs, Switzerland). Sodium chloride and acetic acid (glacial) were purchased at J.T. Baker (Deventer, the Netherlands), sodium acetate trihydrate and sodium hydrogen phosphate dihydrate were purchased at Merck (Darmstadt, Germany). Sodium phosphate dibasic dodecahydrate was obtained by Acros Organics (Geel, Belgium). Pullulan standards were purchased at Polymer Standards Service (Mainz, Germany). Dextran standards were purchased at Fluka (Buchs, Switzerland). Deionized water was purified with a Simpak 2 unit by Millipore (Zug, Switzerland). All used chemicals were of analytical grade. All buffer solutions were prepared using a precision balance METTLER AT250 (Mettler-Toledo, Greifensee, Switzerland). The buffer composition was calculated according to the recipes by Beynon and Easterby [29].

For chromatographic measurements, a HPLC 1100 Series by Agilent Technologies (Santa Clara, CA, USA) was used. The instrument is equipped with an UV-detector and a refractive index detector.

Resins were packed into Tricorn columns purchased at GE Healthcare (Chalfont St Giles, United Kingdom) and Superformance columns by Goetec Labortechnik (Mühltal, Germany). Tricorn columns have a volume of $V \approx 2$ ml and a diameter of $d = 5$ mm. Superformance columns have a volume of $V \approx 20$ ml and a diameter of $d = 16$ mm. 20% mechanical compression of the bed was applied to the resin in those columns. Furthermore, columns by Infochroma (Zug, Switzerland) with a diameter of $d = 4.6$ mm and a volume of $V = 1.0$ ml and columns by YMC (Kyoto, Japan) with a diameter of $d = 7.5$ mm and a volume of $V = 2.2$ ml were used. The latter two columns could not be compressed mechanically.

3. Methods and model

3.1. Pore size distribution

The pore size distribution was measured by inverse size exclusion chromatography (ISEC) [30,31]. In comparison with other techniques for the determination of the pore structure, such as mercury porosimetry or BET measurements, this method has a number of advantages. Particularly, drying of the sample is not necessary. Furthermore, the measurements can be performed directly in the packed column.

ISEC measurements with various dextran and pullulan tracers, as well as protein tracers, were executed under nonadsorbing conditions. The ratio of the accessible liquid volume $V_{t,i}$ for a generic tracer i of specific molecular weight and the total column volume

Table 1
Synthesized Fractogel materials and FractoAIMs and corresponding ligand density. Series 1 includes Fractogels A–E.

Material	ρ_{lig} [μmol/g]
Fractogel EMD SO_3^- (M)	380
Fractogel A	144
Fractogel B	236
Fractogel C	338
Fractogel D	400
Fractogel E	485
FractoAIMs	385

V is used to calculate the total porosity $\epsilon_{t,i}$ accessible to the tracer on the resin:

$$\epsilon_{t,i} = \frac{V_{t,i}}{V} \tag{1}$$

For dextran and pullulan, the average retention volume is estimated from the maximum of the elution peak, because these tracers are actually constituted by a mixture of molecules with different molecular weight. This causes a broadening of the chromatographic peak and therefore an artificial increase of the first moment of the peak. Since protein tracers on the other hand are monodisperse molecules, the retention volume is calculated from the first order moment of the peak.

The bed porosity ϵ_{bed} is estimated by a tracer with a molecular weight that is large enough to be excluded from all pores of the stationary phase. The particle porosity $\epsilon_{p,i}$ is linked to the total porosity $\epsilon_{t,i}$ and the bed porosity ϵ_{bed} by Eq. (2):

$$\epsilon_{t,i} = \epsilon_{bed} + (1 - \epsilon_{bed})\epsilon_{p,i} \tag{2}$$

By measurement of the particle porosity $\epsilon_{p,i}$ of appropriate tracers, it is possible to gather information about the pore size distribution of the stationary phase.

3.2. HETP-values

The concept of the height equivalent to a theoretical plate (HETP) divides the chromatographic column into a number of equilibrium plates. Their height characterizes the separation efficiency of the column and the mass transfer properties of the porous material.

Especially for large molecules such as proteins, diffusion is influencing the path of the tracer through the column. At faster velocities, the chromatogram shows highly asymmetric peaks. Therefore, the HETP values must be calculated from the moments of the peak as follows [32,33]:

$$HETP = L\frac{\sigma^2}{t_R^2} \tag{3}$$

L is a function of the length of the column, σ is the variance and t_R is the average retention time of the peak. Higher moments, such as the variance σ, are very sensitive to measurement errors and noise. In order to minimize this influence, each peak was fitted with a perturbed gamma distribution as proposed by Hulburt and Katz [34]. The fitted peak was then used to calculate the HETP according to Eq. (3).

With the van Deemter equation, the column efficiency HETP is related to axial dispersion D_{ax}, pore diffusion $D_{p,eff}$ and film mass transfer coefficient k_f of the solute in the column as follows [35]:

$$HETP = \frac{2\,D_{ax}}{u} + \frac{2\,u\,d_p}{F}\left(\frac{\epsilon_{p,i}\,F}{\epsilon_{p,i}\,F + 1}\right)^2\left(\frac{d_p}{60\,D_{p,eff}} + \frac{1}{6\,k_f}\right) \tag{4}$$

which applies to the case of a nonadsorbing species. Its derivation as well as a more general representation is given by Guiochon [26]. According to Forrer et al. [36], the term for axial dispersion might be neglected for large molecules such as IgG. The van Deemter equation is a function of the particle diameter d_p, the phase ratio F, defined as

$$F = \frac{1 - \epsilon_{bed}}{\epsilon_{bed}} \tag{5}$$

and the particle porosity $\epsilon_{p,i}$ of the used tracer. The film mass transfer coefficient k_f was calculated according to the equation of Wilson and Geankopolis [37],

$$k_f = 1.09\sqrt[3]{u}\left(\frac{D_m}{\epsilon_{bed}\,d_p}\right)^{2/3} \tag{6}$$

where D_m, the molecular diffusion coefficient, is given by

$$D_m = 8.34 \times 10^{-8}\frac{T}{\eta_S\,\sqrt[3]{MW}} \tag{7}$$

in the particular case of proteins [38]. The viscosity of the solvent (assumed to be the same as 0.1 M sodium chloride solution at 20 °C) is estimated to be $\eta_S = 1.001$ mPa s [39].

The molecular diffusion coefficient for acetone is calculated with the Wilke–Chang equation [40]:

$$D_m = 7.4 \times 10^{-8}\frac{T\sqrt{\Phi_B\,MW}}{\eta_S\,V_n^{0.6}} \tag{8}$$

where the solvent is assumed to be pure water ($MW_{H_2O} = 18.02$ Da). The association factor Φ_B, that accounts for hydrogen bonding of the solvent, was set to $\Phi_B = 2.26$ [41]. The molecular volume V_n of the solute is calculated according to Perry's ($V_n = 73.31$ cm³/mol for acetone) [41].

3.3. Static binding capacity

Static capacity was measured offline. This procedure is convenient, since it allows gaining information about the equilibrium capacity of a material q_{eq} with very little amount of protein and stationary phase. The resin V_{sol} is mixed with a known amount of protein and buffer V_{liq}. Then, the mixture is stirred for two days. After that period of time it is presumed that adsorption equilibrium is reached. The equilibrium capacity q_{eq} is calculated with the initial concentration of protein c_0 and the equilibrium concentration c_{eq} in the supernatant:

$$q_{eq} = \frac{V_{liq}\,(c_0 - c_{eq})}{V_{sol}} \tag{9}$$

Under the selected conditions, the isotherm was rectangular for all materials, i.e. a small concentration of protein ($c_0 < 1$ g/l) in the liquid phase is sufficient to reach the saturation capacity q_∞.

3.4. Dynamic binding capacity

Dynamic binding capacity was measured at 10% breakthrough, i.e. when the outlet protein concentration is 10% of the feed concentration. This was evaluated by testing the feed signal in the UV-detector at a wavelength of 280 nm and then running the breakthrough curve up to a signal of 10% of the original signal. The protein feed concentration was approximately $c_0 \approx 1.7$ g/l. The dynamic binding capacity at 10% breakthrough was calculated as follows:

$$DBC_{10\%} = \frac{t\,A\,u_{lin}\,c}{V} \tag{10}$$

Due to the typically large capacity of these columns and the relatively small feed concentration, the amount of IgG in the liquid phase of the column can be neglected.

Under ideal conditions, that is in the absence of mass transfer resistances, the dynamic binding capacity should be equal to the static binding capacity. Thus, the difference between the two is a way to analyze the extend of mass transfer resistances under loading conditions.

3.5. Modeling approach

For the simulation of breakthrough curves, a general rate model was used [13,42]. The mobile and the stagnant phases are treated separately. All mass balances were set up in dimensionless form. The mass balance for the liquid phase consists of four terms:

$$\frac{\partial c}{\partial \tau} + \frac{\partial c}{\partial \eta} + \epsilon_{p,IgG}\frac{1 - \epsilon_{bed}}{\epsilon_{bed}}St(c - c_p|_{\rho=1}) = \frac{1}{Pe_{ax}}\nabla_{\eta,2}\,c \tag{11}$$

accumulation of the solute in the mobile phase of the column, convection in the axial direction and flux from the mobile to the stagnant phase in the column. The last term on the right-hand side represents axial dispersion along the column. The Stanton number St is defined as the ratio between the characteristic time for convection and the characteristic time for film mass transport $d_p/(6\,k_f)$:

$$St = 6\frac{L\,k_f}{u\,d_p} \tag{12}$$

The axial Peclet number Pe_{ax} gives the ratio between the times for axial dispersion L^2/D_{ax} and convection in the column as follows:

$$Pe_{ax} = \frac{u\,L}{D_{ax}} \tag{13}$$

Danckwerts conditions [43] were used as boundary conditions for Eq. (11):

if $\tau = 0$, then $c = c(0, \eta)$

if $\eta = 0$, then $\dfrac{\partial c}{\partial \eta} = Pe_{ax}(c - c_0)$ $\tag{14}$

if $\eta = 1$, then $\dfrac{\partial c}{\partial \eta} = 0$

The mass balance for the stagnant phase in the general rate model is given by

$$\frac{\partial c_p}{\partial \tau} + \frac{1 - \epsilon_{p,t}}{\epsilon_{p,t}}\frac{\partial q}{\partial \tau} = \frac{1}{Pe}\nabla_{\rho,2}\,c_p \tag{15}$$

where the first term represents accumulation in the stagnant phase with c_p being the concentration of the solute in the stagnant phase and the second represents accumulation of the solute in the solid phase, whereas q is the concentration of adsorbed protein on the stationary phase. The phase ratio is defined through the total porosity of the particle $\epsilon_{p,t}$ (as measured with a small tracer). The term on the right-hand side represents diffusion of the solute across the adsorbent particle. The corresponding particle Peclet number Pe is defined as

$$Pe = \frac{\epsilon_{p,IgG}}{4}\frac{u\,d_p^2}{L\,D_{p,eff}} \tag{16}$$

The boundary conditions of Eq. (15) are given by

if $\tau = 0$, then $c_p = c_p(0, \rho)$

if $\rho = 0$, then $\dfrac{\partial c_p}{\partial \rho} = 0$ $\tag{17}$

if $\rho = 1$, then $\dfrac{\partial c_p}{\partial \rho} = Sh(c - c_p(\rho = 1))$

The Sherwood number is defined as the ratio between the characteristic times for pore diffusion and film mass transfer as follows:

$$Sh = \frac{\epsilon_{p,IgG}}{2}\frac{d_p\,k_f}{D_{p,eff}} \tag{18}$$

4. Results and discussion

As the measurements were performed in various different columns a detailed comparison of the influence of the column geometry and compression on the pore size distribution can be found in supplementary material.

4.1. Analysis of Series 1 (materials with varying ligand density)

4.1.1. Pore size distribution

ISEC measurements for Fractogel EMD SO$_3^-$ (M), Fractogel C and FractoAIMs were performed with dextran tracers, while for all
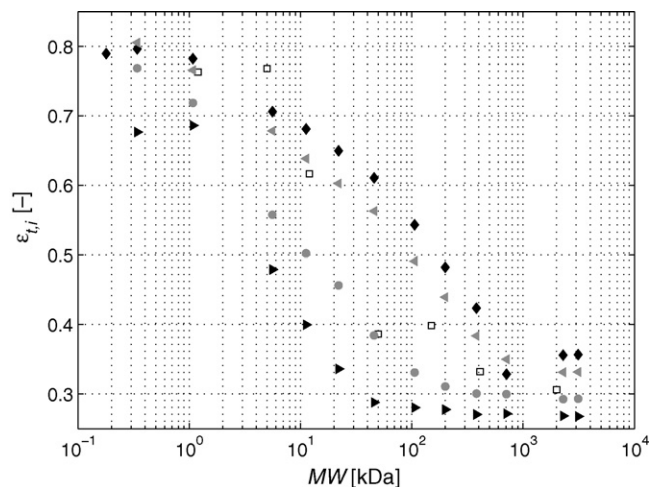

Fig. 1. Comparison of ISEC-measurements for Fractogel A, $\rho_{lig} = 144\,\mu\,\text{mol/g}$ (♦), Fractogel B, $\rho_{lig} = 236\,\mu\,\text{mol/g}$ (◄), Fractogel C, $\rho_{lig} = 338\,\mu\,\text{mol/g}$ (□), Fractogel D, $\rho_{lig} = 400\,\mu\,\text{mol/g}$ (●) and Fractogel E, $\rho_{lig} = 485\,\mu\,\text{mol/g}$ (►).

other materials pullulan was used. The measurements were performed under nonadsorbing conditions, namely 50 mM phosphate buffer pH 7 with 0.5 M sodium chloride . Nonadsorbing conditions have been checked by repeating the same experiment at different salt concentrations. This check, however, cannot fully exclude the presence of some unspecific binding (e.g. hydrophobic interaction).

The bed porosity was determined with a tracer with a molecular weight of 2000 kDa (hydrodynamic radius $r_h = 37.2$ nm, calculated according to DePhillips and Lenhoff [44]) that is totally excluded from the pores. The total porosity of each material was calculated with a dextran tracer with a molecular weight of 1.2 kDa or a pullulan tracer with a molecular weight of 1.1 kDa, respectively. It is assumed that a molecule of this size can penetrate all relevant pores of the stationary phase.

For all materials, protein tracers, especially IgG and HSA, were also tested. Those measurements were performed under nonadsorbing conditions, namely 20 mM acetate buffer pH 5 with a minimum of 0.5 M sodium chloride.

In Fig. 1, the pore accessibilities for different materials (Series 1, see Table 1) measured in the Goetec column are shown as a function of the dextran/pullulan molecular weight. As all materials are based on the same support, they should have the same pore structure. However, since the ligands block part of the pores, it follows that pore accessibility decreases with ligand density. In particular, Fig. 1 shows that the transition region of the ISEC curve is shifted depending on the ligand density. We see for example that Fractogel E will not show a good performance with respect to IgG purification, since the porosity of the tracer with a molecular weight of 46 kDa is already equal to the bed porosity, meaning that IgG, which has a molecular weight of 144 kDa, is probably totally excluded from the pores and therefore does not access the ligands in the pores. In all cases a plateau is reached for the largest tracers, thus confirming the choice of the 2000 kDa tracer for the estimation of the bed porosity.

The particle porosities of IgG for the different materials discussed above are compared in Fig. 2 as a function of the ligand density. It is seen that the particle porosity for IgG is highly influenced by the ligand density, as the porosity changes from 42% to 5% for IgG in the analyzed range.

A comparison of the porosity measurements for Fractogel C (Series 1) and the benchmark material Fractogel EMD SO$_3^-$ (M), which both have a similar ligand density (see Table 1), is shown in Table 2. It is seen that the bed porosity of the two materials is nearly the same. However, the particle porosity of IgG on Fractogel EMD SO$_3^-$ (M) is slightly higher, indicating either a slightly differ-
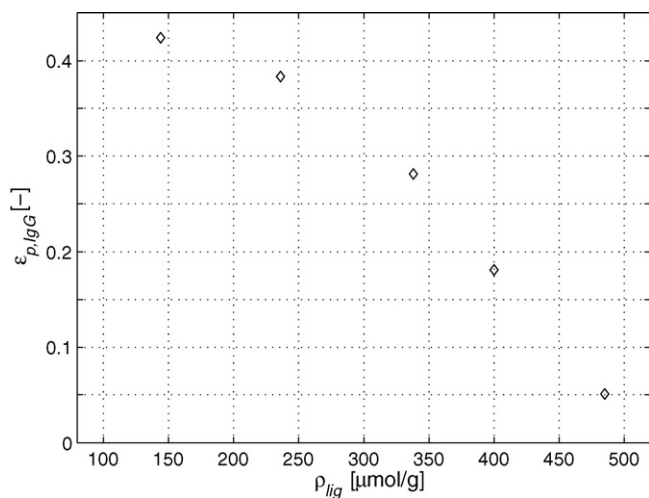
Fig. 2. Particle porosity of IgG as a function of the ligand density.

Table 2
Total and particle porosity of various tracers for Fractogel EMD SO$_3^-$ (M) and Fractogel C measured on column Goetec.

Material	ϵ_{bed}	$\epsilon_{t,IgG}$	$\epsilon_{p,IgG}$	ϵ_t	$\epsilon_{p,t}$
Fractogel EMD SO$_3^-$ (M)	0.32	0.54	0.33	0.73	0.61
Fractogel C	0.31	0.50	0.28	0.76	0.66

ent pore structure of the two materials or a slightly different ligand distribution in the pores or a combination of the two effects.

4.1.2. HETP values

Measurements for the estimation of the *HETP* were conducted under nonadsorbing conditions with 20 mM acetate buffer pH 5 with a minimum of 0.5 M sodium chloride. As for the ISEC measurements, the Goetec column with a volume of 20 ml was used. The *HETP* was measured in the range of linear velocity values of $u_{lin} = 9 - 90$ cm/h, whereas the latter value corresponds to the maximum flow rate for the HPLC pump. Fig. 3 shows *HETP* of various tracers as a function of the linear velocity for Fractogel C. It is seen that the van Deemter curve is almost flat with small values of *HETP* for the smallest tracer, i.e. acetone. As expected, there is only little pore diffusion limitation in the column for this small molecule. For proteins, the influence of pore diffusion becomes significant. The largest protein IgG has the highest *HETP* values for all measured
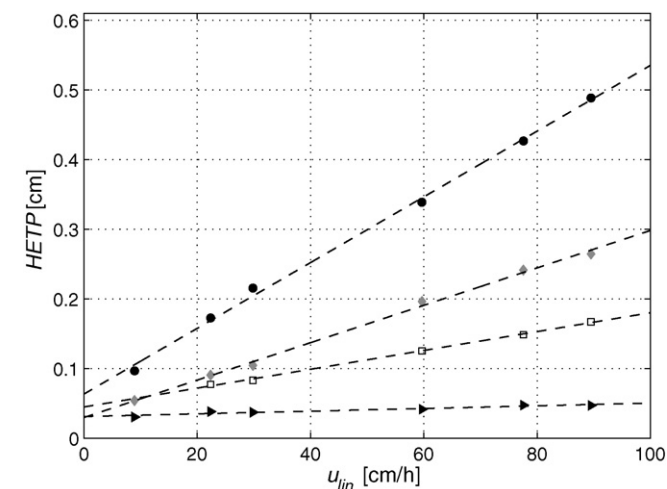

Fig. 3. *HETP* values for Fractogel C: acetone (▶), myoglobin (□), HSA (♦) and IgG (●).

velocities. The number of theoretical plates is highly dependent on the velocity ranging from 20 to 103 plates for the used column. These results confirm the need for optimization of mass transport effects in such columns and explain the large dependence of the dynamic binding capacity on the linear velocity that is typically observed for large proteins.

As described in Eq. (4), the information from the van Deemter plot can be used to estimate the effective pore diffusion. Note that Fig. 3 shows the *HETP* values as a function of the linear velocity u_{lin}, whereas the values of the pore effective diffusivity $D_{p,eff}$ (Eq. (4)) are calculated with the interstitial velocity u ($u_{lin} = \epsilon_{bed}u$). The obtained results are reported in Table 3 for different molecules. As expected, it can be observed that the pore effective diffusivity decreases with increasing molecular weight of the tracer. Note that the ratio between molecular and pore effective diffusivity increases with the protein size, thus indicating that the transport becomes more and more hindered with increasing protein size. For a comparison, in the last column of Table 3, the pore effective diffusivity values measured by Forrer et al. on Fractogel EMD SE Hicap (M) are reported [36]. These numbers correspond rather well with the values measured in this work.

For each of the Series 1 materials, the van Deemter plot has been produced (not shown) and the corresponding slope *HETP*/u measured as reported in Table 4. From such values, the pore diffusivity has been computed using Eq. (4) and the particle porosity values of IgG measured in Fig. 2. It appears that most of the variation of the slope *HETP*/u is due to different values for the particle porosity of IgG while the pore diffusivities exhibit a not always coherent trend. Note, that the van Deemter equation (Eq. (4)) is in fact a strong function of the particle porosity of the target molecule and not only of its pore diffusivity. Indeed, it is seen that Fractogel A and B have larger pore effective diffusivities than the benchmark material Fractogel EMD SO$_3^-$ (M). As these two materials have a significantly lower ligand density than the benchmark material, the corresponding accessible pores are wider which leads to pore effective diffusivities that are approximately 50% larger. However, when looking at higher ligand density values, this trend is not confirmed. It should be noted however, that for example for Fractogel E, the ligand density is so large and the accessible porosity towards IgG is so low (Fig. 2) that talking about pore diffusivity is hardly possible and therefore the effect of measurement errors becomes strong.

4.1.3. Static binding capacity

Static capacity was measured offline in stirred beakers. A mixture of 50% resin and 50% buffer (20 mM acetate buffer with 30 mM sodium chloride at pH 5) was agitated for two days with a known amount of IgG. The IgG concentration of the supernatant was then analyzed and the corresponding adsorbed equilibrium concentration was calculated according to Eq. (9).

The static binding capacity of IgG for the materials of Series 1 is shown in Fig. 4 in terms of the adsorption equilibrium isotherm. For all measured materials it exhibits a characteristic rectangular shape, i.e. saturation conditions are achieved already with very small IgG concentrations in the liquid phase.

The saturation capacity q_∞ as a function of the ligand density is shown in Fig. 5. The binding capacity reaches a maximum at a ligand density of approximately $\rho_{lig} \approx 400\,\mu$mol/g. This result is discussed in detail later in the context of the dynamic binding capacity data.

It is worth mentioning that since this method uses only very small amounts of protein and resin, the error of the absolute values for the saturation capacity could be large. However, part of the dataset was measured in duplicate and a maximum error of 15% was measured.

Forrer et al. measured the saturation capacity for Fractogel EMD SE Hicap (M) with Gammanorm with 20 mM acetate buffer with

Table 3
Film mass transfer coefficient k_f, molecular diffusivity D_m, pore effective diffusivity $D_{p,eff}$ and ratio between molecular and pore effective diffusivity $D_m/D_{p,eff}$ for selected tracers on Fractogel C. The film mass transfer coefficient was calculated at a velocity of $u = 0.04$ cm/min. As a comparison, the last column shows the pore effective diffusivity $D_{p,eff}$ as measured by Forrer et al. on Fractogel EMD SE Hicap (M) [36].

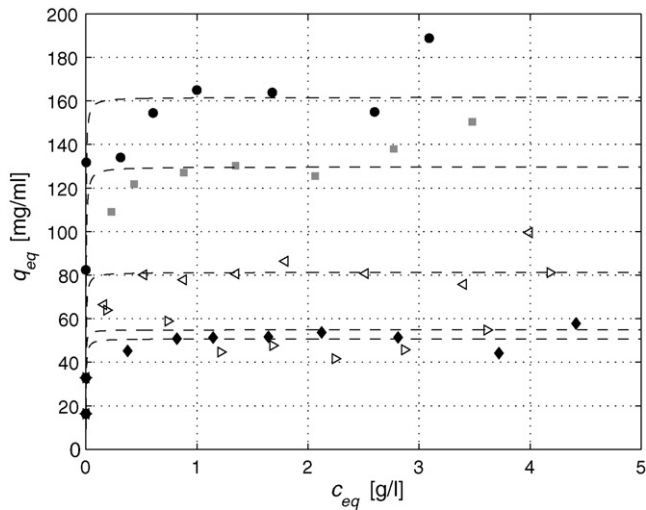| Tracer	k_f [cm/s]	D_m [cm^2/s]	$D_{p,eff}$ [cm^2/s]	$D_m/D_{p,eff}$	$D_{p,eff}$ [cm^2/s]
Acetone	1.14×10^{-2}	1.05×10^{-5}	1.63×10^{-6}	6.46	1.09×10^{-6}
Myoglobin	2.27×10^{-3}	9.38×10^{-7}	1.58×10^{-7}	5.95	1.60×10^{-7}
HSA	1.69×10^{-3}	6.04×10^{-7}	3.82×10^{-8}	15.80	5.69×10^{-8}
IgG	1.42×10^{-3}	4.66×10^{-7}	1.85×10^{-8}	25.23	2.31×10^{-8}

Fig. 4. Adsorption equilibrium isotherm for IgG with 20 mM acetate buffer pH 5 with 0.03 M sodium chloride for Fractogel A, $\rho_{lig} = 144\,\mu$ mol/g (◆), Fractogel B, $\rho_{lig} = 236\,\mu$ mol/g (◁), Fractogel C, $\rho_{lig} = 338\,\mu$ mol/g (■), Fractogel D, $\rho_{lig} = 400\,\mu$ mol/g (●) and Fractogel E, $\rho_{lig} = 485\,\mu$ mol/g (◁). The dashed lines represent Langmuir isotherm fits of the data.
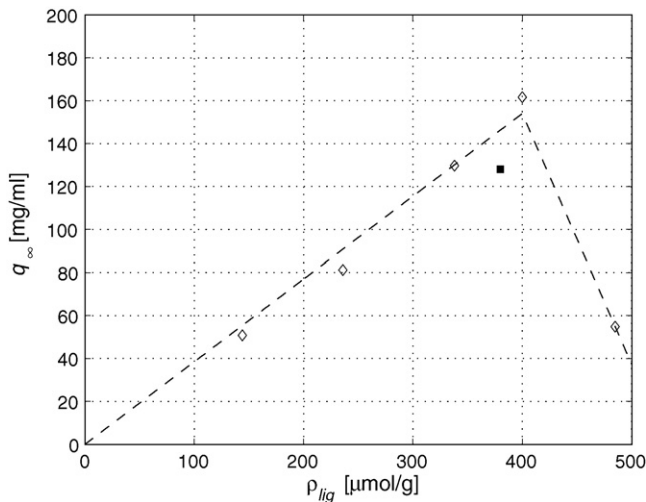

Fig. 5. Saturation capacity q_∞ as a function of the ligand density for Series 1 (◇). Fractogel EMD SO$_3^-$ (M) (■) is also shown.

Table 4
Slope of the van Deemter curve $HETP/u$ and pore effective diffusivity $D_{p,eff}$ for the benchmark material Fractogel EMD SO$_3^-$ (M) and Series 1 for IgG.

Material	ρ_{lig} [μmol/g]	$HETP/u$ [s]	$D_{p,eff}$ [cm^2/s]
Benchmark	380	3.61	3.28×10^{-8}
Fractogel A	144	3.42	4.69×10^{-8}
Fractogel B	236	2.87	5.12×10^{-8}
Fractogel C	338	5.20	1.85×10^{-8}
Fractogel D	400	2.72	2.25×10^{-8}
Fractogel E	485	0.40	3.05×10^{-8}

0.05 M sodium chloride [36], hence with a modifier concentration slightly higher than in the experiments presented here. However, Forrer calculated a saturation capacity of $q_\infty = 156$ g/l. This value is 22% higher than the value measured in this paper for Fractogel EMD SO$_3^-$ (M) ($q_\infty = 128$ g/l). A similar difference of about 20% in the capacities of these two resins was reported earlier in the literature [7].

4.1.4. Dynamic binding capacity

These experiments were conducted using 20 mM acetate buffer with 30 mM sodium chloride at pH 5 which are the same conditions used above for the determination of the static binding capacity. The protein was eluted with 20 mM acetate buffer with 1 M sodium chloride at pH 5. After each breakthrough curve cleaning in place (CIP) was done with 0.25 M sodium hydroxide solution.

Dynamic binding capacity at 10% was measured for all materials listed in Table 1 at two different velocities ($u_{lin} = 181$ cm/h and $u_{lin} = 361$ cm/h). The corresponding breakthrough curves are shown in Fig. 6 for Fractogel C only.

The obtained values of $DBC_{10\%}$ computed through Eq. (10) for the Series 1 materials and for Fractogel EMD SO$_3^-$ (M) at the two selected velocities are shown in Fig. 7 together with the static binding capacity values discussed above. In all cases a maximum of the dynamic or static binding capacity is seen as a function of the ligand density. This maximum is influenced by the amount of available ligands on the one hand and by the accessible surface area for IgG on the other hand. If a material is functionalized with a large amount of ligands, the number of possible binding sites is increased, while at the same time, the number of accessible binding sites is decreased, because the ligands block part of the pores that IgG cannot enter anymore.

It is worth noting, that the maximum dynamic binding capacity is not necessarily at the same ligand density value for all flow rates and in particular at static conditions. Fig. 7 shows that the maximum for the static binding capacity is at a ligand density of
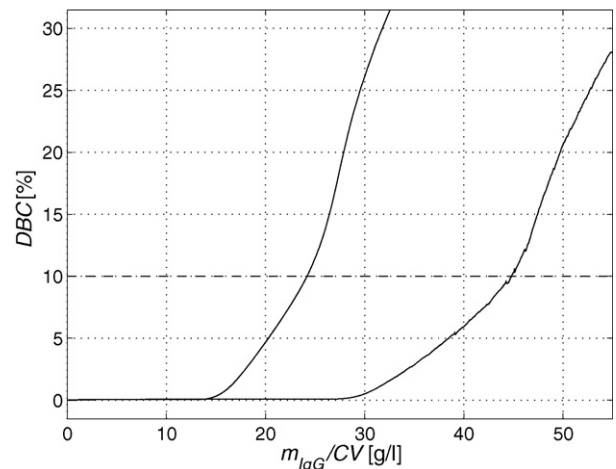

Fig. 6. Breakthrough curves for different flowrates for Fractogel C: $u_{lin} = 361$ cm/h (left), $u_{lin} = 181$ cm/h (right). The feed concentration was c_{IgG}=1.46 g/l.
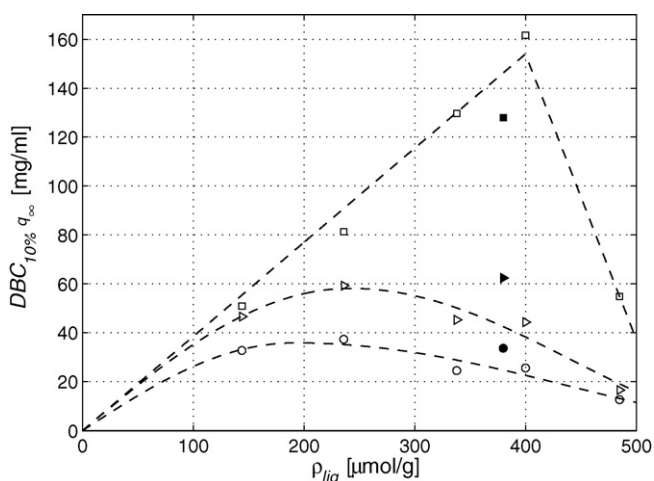
Fig. 7. Dynamic binding capacity at 10% breakthrough $DBC_{10\%}$: $u_{lin} = 181$ cm/h ($\triangleleft$) and $u_{lin} = 361$ cm/h ($\circ$). The saturation capacity q_∞ is measured in batch mode ($\square$). The empty symbols represent Series 1, whereas the data for Fractogel EMD SO$_3^-$ (M) is shown as filled symbols.

$\rho_{lig} \approx 400\,\mu$ mol/g, whereas it shifts to lower ligand densities for dynamic conditions. This behavior can be explained as the trade-off between the static capacity and the diffusion limitations that are becoming more pronounced at larger flow rates, thus hindering the access to all the available capacity. This is further complicated by the fact that as discussed above, the ligand density has an independent direct effect in lowering the pore diffusivity. This means that it is important to tune the ligand density for the targeted loading velocity in order to reach an optimal performance.

A simple way to compute the fraction of ligands which is actually accessible for IgG under certain conditions is to assume that this is equal to the fraction of pore volume which is actually accessible for IgG under the same conditions that is

$$\frac{\rho_{lig}^{acc}}{\rho_{lig}} = \frac{\epsilon_{t,IgG} - \epsilon_{bed}}{\epsilon_t - \epsilon_{bed}} \qquad (19)$$

If we now replot the $DBC_{10\%}$ values as a function of the so converted accessible ligand density ρ_{lig}^{acc}, as shown in Fig. 8, we find the
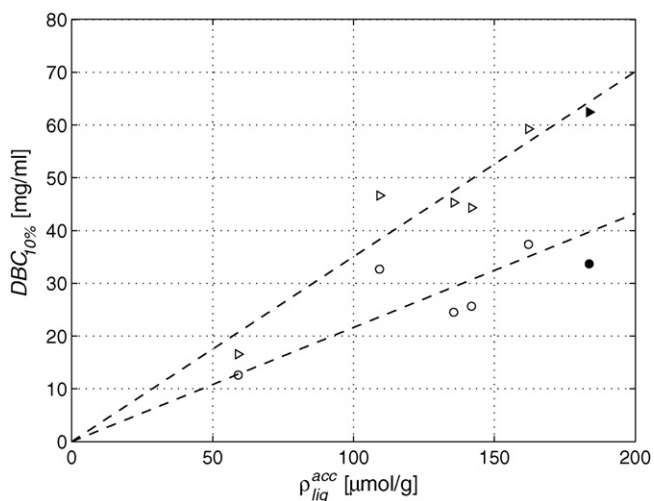

Fig. 8. Dynamic binding capacity at 10% breakthrough as a function of the accessible ligand density ρ_{lig}^{acc}: $u_{lin} = 181$ cm/h ($\triangleleft$) and $u_{lin} = 361$ cm/h ($\circ$). The empty symbols represent Series 1, whereas the data for Fractogel EMD SO$_3^-$ (M) is shown as filled symbols.

expected trend of the dynamic binding capacity increasing linearly with the ligand density. This is because we consider only the fraction of ligands here which is accessible and not their total number (as in Fig. 7). The slope of the straight line increases when the velocity decreases due to the presence of mass transport resistances.

Note on the other hand that such a linear behavior is not exhibited by the static binding capacity data in Fig. 5. This should not be surprising since the concept of accessibility has to be understood in the time frame of a chromatographic run, i.e. some minutes. On the contrary, in static experiments we wait days in order to reach equilibrium conditions and therefore some pores which were not accessible for IgG under dynamic conditions may become accessed.

4.2. Development of a new ion exchange resin: FractoAIMs

Based on the understanding derived from the analysis of the Series 1 materials, a new stationary phase was designed. The following criteria were set:

- the material should have an optimal ligand density to maximize the dynamic binding capacity.
- the material should have a large pore accessibility to IgG, in order achieve fast mass transport rates.
- the material should have a high rigidity so as to tolerate high eluentvelocities (i.e. productivities).

FractoAIMs is the material, that was developed in order to meet those criteria. Mass transfer resistances have been reduced first by an arbitrary reduction of the particle size from $d_p = 65\,\mu$m to $d_p = 40\,\mu$m. All the other properties are reported in Section 2. In order to operate the material with high flow rate also under preparative conditions, the particles are designed to be especially rigid. The ligand density of FractoAIMs (listed in Table 1) is selected to lead to high dynamic biding capacities. In the following, FractoAIMs is compared to the benchmark material Fractogel EMD SO$_3^-$ (M) . Both materials were packed into YMC columns.

The pore size distribution of FractoAIMs and Fractogel EMD SO$_3^-$ (M) is very similar, whereas the pore accessibility of proteins is about 10% larger for FractoAIMs in comparison with Fractogel EMD SO$_3^-$ (M). HETP data for FractoAIMs are roughly only 50% of the HETP-values for Fractogel EMD SO$_3^-$ (M). However, this is of course due to significantly shorter characteristic time for diffusion, because of the smaller particles for FractoAIMs. The calculated pore effective diffusivity gives very similar values for both materials that are in good agreement with literature data. The static binding capacity of FractoAIMs was determined according to the previously described method and is the same as the static binding capacity of Fractogel EMD SO$_3^-$ (M). A detailed comparison of the pore size distribution, the diffusivities and the static binding capacities for FractoAIMs and Fractogel EMD SO$_3^-$ (M) can be found in supplementary material.

As shown in Fig. 9, the dynamic binding capacity is two times larger for FractoAIMs than for Fractogel EMD SO$_3^-$ (M) for the fastest velocities. The ligand density and the static binding capacity as well as the pore effective diffusivity of the two materials are similar. Therefore this result underlines the importance to reduce the particle size and increase the pore accessibility towards the target molecule in order to achieve larger mass transfer rates and thus better values for the dynamic binding capacity. Of course, a material with reduced particle size exhibits a larger pressure drop, and therefore a suitable compromise has to be found.

Note that the lines in Fig. 9 serve to guide the eye and do not represent the actual dependence of the dynamic binding capacity on the velocity. As the static capacity is nearly the same for both materials, the two curves must converge to the same value at low velocities, because mass transfer resistances under these
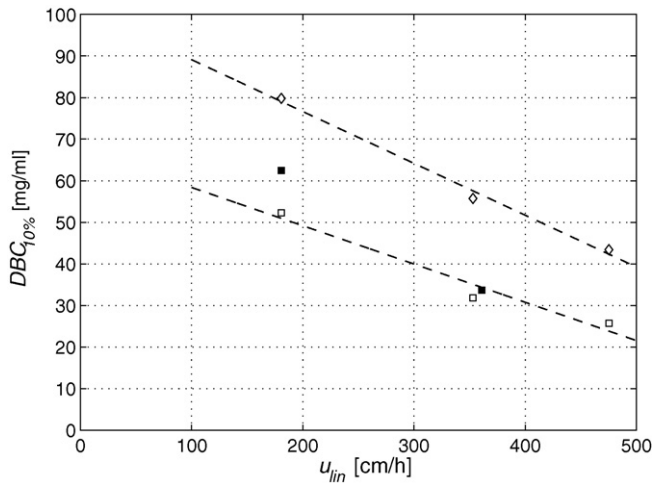
Fig. 9. Dynamic binding capacity at 10% breakthrough for IgG on FractoAIMs ($\diamond$) and Fractogel EMD SO$_3{}^-$ (M) ($\square$) measured on the YMC column. The data set from the previous section on the Infochroma column for Fractogel EMD SO$_3{}^-$ (M) ($\blacksquare$) is also shown.

conditions are not limiting any more. The diverging behavior of the lines is therefore an artefact caused by the small number of measured points. The true dependence of the dynamic binding capacity on the velocity is shown later with simulations.

4.3. Simulation

The behavior of the two materials under examination, i.e. Fractogel EMD SO$_3{}^-$ (M) and FractoAIMs, has been investigated also using the general rate model presented in Section 3.5. One important application of the developed model is to predict values of the dynamic binding capacity. This would provide a very valuable tool for screening stationary and mobile phases for a given industrial purification process. For this goal, it is a prerequisite to find a procedure for the quick estimation of model parameter values that requires very small amounts of protein and stationary phase. A possible strategy is presented in the following.

Parameter values were fitted to the general rate model in multiple separate regressions. All regressions were done for both Fractogel EMD SO$_3{}^-$ (M) and FractoAIMs. First, the bed porosity was fitted to ISEC data (see supplementary material). Then, the porosity for IgG and the axial diffusion coefficient in the column (in terms of axial Peclet number Pe_{ax}) were regressed with experimental data under nonadsorbing conditions (see supplementary material). Literature correlations (Eqs. (6) and (7)) were used to estimate the mass transfer coefficients and the Stanton number St (Eq. (12)). The particle Peclet number Pe was calculated according to Eq. (16), whereas the pore effective diffusivity $D_{p,eff}$ was estimated from the van Deemter plot (see supplementary material) according to Eq. (4). All relevant parameters for both materials are listed in Table 5.

Table 5
Parameter values of the general rate model for Fractogel EMD SO$_3{}^-$ (M) and FractoAIMs. Pe_{ax}, St, k_f and Pe are listed at a velocity of u_{lin} = 361 cm/h.

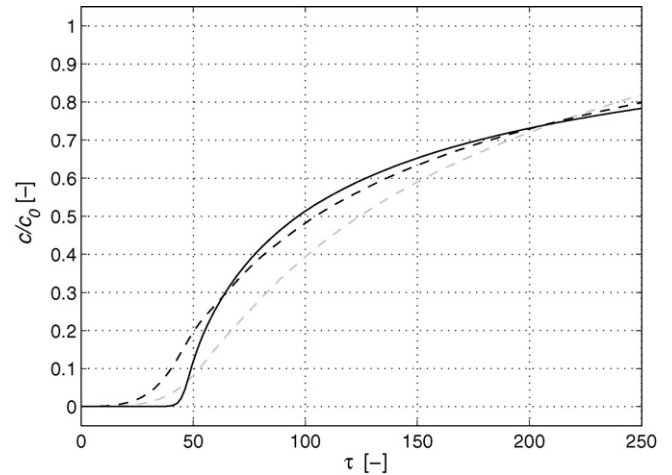| Parameter	Fractogel EMD SO$_3{}^-$ (M)	FractoAIMs
ϵ_{bed}	0.43	0.43
ϵ_t	0.76	0.78
$\epsilon_{t,IgG}$	0.63	0.65
Pe_{ax}	555	1738
St	39	88
k_f	1.97×10^{-3}	2.30×10^{-3}
Pe (from HETP)	4.15	2.01
Pe (from simulation)	6.26	3.20
q_∞ [g/l]	110	111

Fig. 10. Experimental breakthrough curve at u_{lin} = 361 cm/h for IgG on Fractogel EMD SO$_3{}^-$ (M) (solid black line), prediction (dashed grey line) and with fit of Peclet number (dashed black line).

Using these parameter values together with values for the static binding capacity from batch experiments, the breakthrough curves, shown in Figs. 10 and 11 for the two materials, have been predicted and compared with the corresponding experimental data. Considering the uncertainties behind such an entirely predictive procedure, the comparison is satisfactory.

In order to improve the fit, the Peclet number (and therefore the pore effective diffusion coefficient $D_{p,eff}$) was used as an adjustable parameter in the general rate model. A better simulation result is achieved with $D_{p,eff} = 2.32 \times 10^{-8}$ cm^2/s for FractoAIMs and $D_{p,eff} = 2.72 \times 10^{-8}$ cm^2/s for Fractogel EMD SO$_3{}^-$ (M), as also shown in Figs. 10 and 11, respectively. This represents a reduction of about 36% in both cases with respect to the value estimated from the van Deemter plot.

This can be explained by the fact that particle porosities towards the target molecule (and therefore mass transfer parameters) can be reduced by other factors that are not included in the model such as the ionic strength of the mobile phase and the protein loading on the stationary phase. In particular, Forrer et al. found that a decrease in the modifier concentration (i.e. sodium chloride) leads to a decrease in the particle porosity of tracers [45]. In this work the total porosities and the particle porosity of IgG as well as the mass transfer resistances have been measured using at least 0.5 M
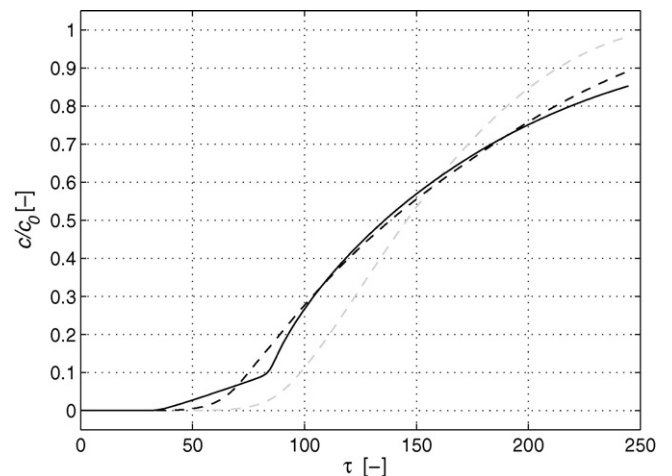

Fig. 11. Experimental breakthrough curve at u_{lin} = 361 cm/h for IgG on FractoAIMs (solid black line), prediction (dashed grey line) and with fit of Peclet number (dashed black line).
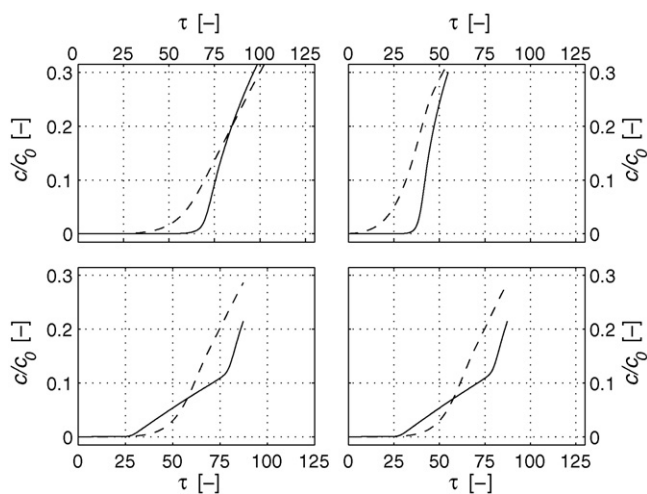
Fig. 12. Experimental breakthrough curve for IgG (solid line) and prediction (dashed line): Fractogel EMD SO$_3^-$ (M) at $u_{lin} = 181$ h (top left), Fractogel EMD SO$_3^-$ (M) at $u_{lin} = 475$ cm/h (top right), FractoAIMs at $u_{lin} = 181$ cm/h (bottom left), FractoAIMs at $u_{lin} = 475$ cm/h (bottom right).

sodium chloride in the buffer in order to ensure nonadsorbing conditions. On the other hand, the ionic strength was much lower in the breakthrough experiments in Figs. 10 and 11.

More important, Forrer et al. and Melter et al. have shown that the pore accessibility is strongly decreasing as a function of loading, i.e. in conditions typical of our breakthrough experiments [42,13]. Both effects are neglected in the model used here which assumes a constant pore diffusion rate coefficient. These aspects need to be addressed in future work in order to improve the prediction capabilities of this model.

A possible application of the model developed above for process development is shown in Fig. 12 where the breakthrough curves are predicted for both materials at two different velocity values $u_{lin} = 181$ cm/h and $u_{lin} = 475$ cm/h. There is an acceptable agreement between simulation and experimental data, although the prediction of the $DBC_{10\%}$ based on these simulations would not be fully satisfactory. For this, the model improvements discussed above are probably necessary.

Finally, in order to analyze the influence of the particle size on the dynamic binding capacity more closely, the dynamic binding capacity of both materials is simulated for 14 different velocities in the range of $u_{lin} = 15 - 3000$ cm/h (Fig. 13).
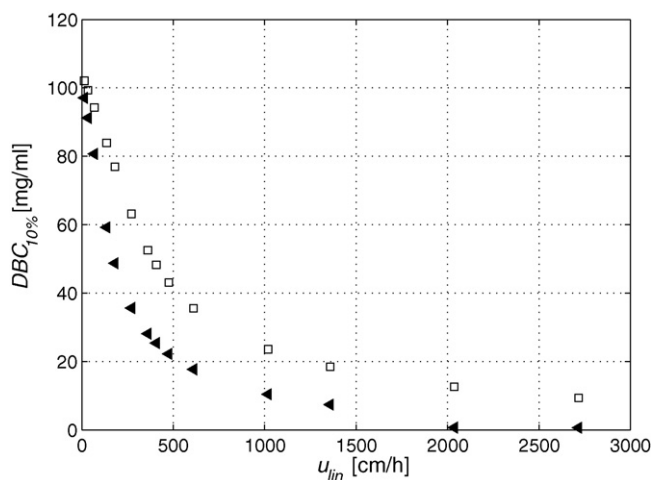

Fig. 13. Simulation of dynamic binding capacity for Fractogel EMD SO$_3^-$ (M) (◄) and FractoAIMs (□).

This study is hardly possible experimentally, because of high protein consumption of each breakthrough curve and because there are no materials available that can be operated at velocities significantly higher than $u_{lin} = 400$ cm/h. As expected, a strong influence of the particle size on the dynamic binding capacity as a function of the applied flow rate is observed. At very slow loading velocities ($u_{lin} \ll 100$ cm/h), the dynamic binding capacity is almost independent of the particle size. However, already at a linear velocity of $u_{lin} = 181$ cm/h, the dynamic binding capacity of FractoAIMs is 35% higher than that of Fractogel EMD SO$_3^-$ (M). With increasing loading velocities (above 500 cm/h), this difference increases even further.

5. Conclusion

It has been shown that the ligand density is an important parameter in determining the performance of a chromatographic material. It affects not only the saturation capacity of the material but also its pore structure, thus rendering the pores more or less accessible to large molecules and changing also the corresponding pore diffusivities. All these factors play a strong role for the determination of the dynamic binding capacity and in general, they conflict with each other. An optimal ligand density arises as the compromise between a high ligand density for large saturation capacities and a low density for well accessible pores and large mass transfer rates. However, this optimum is a function of the target molecule as well as process conditions such as the loading velocity.

As an example of the procedure for the design of an improved stationary phase for protein purification, a new material was presented that has a high pore accessibility for IgG together with a small particle size. Because of the rigidity of the particles, the material can be operated at high flow rates. Therefore, mass transfer resistances can be reduced while keeping high flow rates. This procedure increases the productivity of the stationary phase and speeds up the downstream process.

A chromatographic column model has been developed and the corresponding parameters have been evaluated using chromatographic experiments under nonadsorbing conditions and simple batch experiments which need very small amounts of IgG and other tracer molecules. The obtained results are encouraging, although in order to obtain quantitative results which can be used for process screening, the model would require some further improvement. In particular, the effect of protein loading on pore diffusivity should be accounted for. The objective of this model is to predict the column behavior and hence the dynamic binding capacity. This would provide a useful tool in the phase of process screening at the beginning of the development of protein purification processes.

Nomenclature

A	cross-section of the column [cm^2]
A	parameter for the calculation of the HETP-value [cm]
B	parameter for the calculation of the HETP-value [cm]
C	parameter for the calculation of the HETP-value [s/cm]
c	concentration of the solute [g/l]
c_{eq}	equilibrium concentration [g/l]
c_p	concentration of the solute in the liquid phase of the particle [g/l]
c_0	feed concentration [g/l]
CV	column volume [ml]
D_{ax}	axial dispersion coefficient [cm^2/s]
D_m	molecular diffusion coefficient [cm^2/s]
$D_{p,eff}$	pore effective diffusion coefficient [cm^2/s]
d	diameter [mm]

d_p	particle diameter [cm]
DBC	dynamic binding capacity [g/l]
F	phase ratio
H	Henry coefficient
HETP	height equivalent of a theoretical plate [cm]
HSA	human serum albumin
IgG	immunoglobulin G
ISEC	inverse size exclusion chromatography
$K_{d,IgG}$	pore accessibility for IgG
k_f	film mass transfer coefficient [cm/s]
L	column length [cm]
MW	molecular weight [Da]
m	mass [mg]
Pe	Peclet number
Pe_{ax}	axial Peclet number
Q	flow rate [ml/min]
q_{eq}	equilibrium capacity [g/l]
q_∞	saturation capacity [g/l]
r	radial position in the particle [cm]
r_h	hydrodynamic radius [nm]
r_p	pore radius [Å]
Sh	Sherwood number
St	Stanton number
T	Temperature [K]
t	time [min]
u	interstitial velocity ($u = Q/\epsilon_{bed} A$) [cm/s]
u_{lin}	linear velocity ($u = Q/A$) [cm/min]
V	volume [ml]
z	axial position in the column [cm]
ϵ	porosity of a tracer
η	dimensionless axial position
η_s	solvent viscosity [mPa s]
ρ	dimensionless radial position
ρ_{lig}	ligand density [µmol/g]
σ	variance of the peak [min]
τ	dimensionless time
Φ_B	association factor of the solvent in the Wilke–Change equation

Acknowledgement

Appendix A. Supplementary data

Supplementary data associated with this article can be found, in the online version, at doi:10.1016/j.chroma.2010.02.002.

References

[1] U. Gottschalk, Biopharm Int. 18 (6) (2005) 42.
[2] D. Low, R. O'Leary, N.S. Pujar, J. Chromatogr. B: Anal. Technol. Biomed Life Sci. 848 (1) (2007) 48.
[3] A.C.A. Roque, C.R. Lowe, M.A. Taipa, Biotechnol. Progr. 20 (3) (2004) 639.
[4] A.A. Shukla, B. Hubbard, T. Tressel, S. Guhan, D. Low, J. Chromatogr. B: Anal. Technol. Biomed. Life Sci. 848 (1) (2007) 28.
[5] D.S. Terman, J.H. Bertram, Eur. J. Cancer Clin. Oncol. 21 (10) (1985) 1115.
[6] D.K. Follman, R.L. Farner, J. Chromatogr. A 1024 (1–2) (2004) 79.
[7] A. Stein, A. Kiesewetter, J. Chromatogr. B: Anal. Technol. Biomed. Life Sci. 848 (1) (2007) 151.
[8] Y. Kato, K. Nakamura, T. Kitamura, M. Hasegawa, H. Sasaki, J. Chromatogr. A 1036 (1) (2004) 45.
[9] L. Guerrier, P. Girot, W. Schwartz, E. Boschetti, Bioseparation 9 (4) (2000) 211.
[10] E. Boschetti, J. Biochem. Biophys. Methods 49 (1–3) (2001) 361.
[11] W. Schwartz, D. Judd, M. Wysocki, L. Guerrier, E. Birck-Wilson, E. Boschetti, J. Chromatogr. A 908 (1–2) (2001) 251.
[12] A. Franke, T. Müller-Späth, M. Morbidelli, Application of mixed mode resins for the purification of antibodies, in preparation.
[13] L. Melter, A. Butté, M. Morbidelli, J. Chromatogr. A 1200 (2) (2008) 156.
[14] A. Staby, I.H. Jensen, I. Mollerup, J. Chromatogr. A 897 (1–2) (2000) 99.
[15] A. Staby, I.H. Jensen, J. Chromatogr. A 908 (1–2) (2001) 149.
[16] A. Staby, M.B. Sand, R.G. Hansen, J.H. Jacobsen, L.A. Andersen, M. Gerstenberg, U.K. Bruus, I.H. Jensen, J. Chromatogr. A 1034 (1–2) (2004) 85.
[17] A. Staby, M.B. Sand, R.G. Hansen, J.H. Jacobsen, L.A. Andersen, M. Gerstenberg, U.K. Bruus, I.H. Jensen, J. Chromatogr. A 1069 (1) (2005) 65.
[18] A. Staby, J.H. Jacobsen, R.G. Hansen, U.K. Bruus, I.H. Jensen, J. Chromatogr. A 1118 (2) (2006) 168.
[19] A. Staby, R.H. Jensen, M. Bensch, J. Hubbuch, D.L. Dunweber, J. Krarup, J. Nielsen, M. Lund, S. Kidal, T.B. Hansen, I.H. Jensen, J. Chromatogr. A 1164 (2007) 82.
[20] S. Ghose, B. Hubbard, S.M. Cramer, J. Chromatogr. A 1122 (1–2) (2006) 144.
[21] B.C.S. To, A.M. Lenhoff, J. Chromatogr. A 1141 (2) (2007) 191.
[22] F. Helfferich, Ionenaustauscher Band I, Verlag Chemie, Weinheim/Bergstraße, 1959.
[23] D.L. Wu, R.R. Walters, J. Chromatogr. 598 (1) (1992) 7.
[24] S.P. Zhang, Y. Sun, J. Chromatogr. A 964 (1–2) (2002) 35.
[25] J.F. Langford, X.K. Xu, Y. Yao, S.F. Maloney, A.M. Lenhoff, J. Chromatogr. A 1163 (1–2) (2007) 190.
[26] G. Guiochon, A. Felinger, D.G. Shirazi, A.M. Katti, Fundamentals of Preparative and Nonlinear Chromatography, Academic Press, Boston, MA, USA, 2006.
[27] K. Kaczmarski, D. Antos, J. Chromatogr. A 756 (1–2) (1996) 73.
[28] W. Müller, J. Chromatogr. 510 (1990) 133.
[29] R. Beynon, J. Easterby, Buffer Solutions: The Basics, Oxford University Press, Oxford, Great Britain, 1996.
[30] I. Halasz, K. Martin, Berichte der Bunsen-Gesellschaft-Phys. Chem. Chem. Phys. 79 (9) (1975) 731.
[31] I. Halasz, K. Martin, Angew. Chem. Ed. in English 17 (12) (1978) 901 (in English).
[32] S. Yamamoto, K. Nakanishi, R. Matsuno, Ion-exchange Chromatography of Proteins, Marcel Dekker, New York, NY, USA, 1988.
[33] G. Carta, A.R. Ubiera, T.M. Pabst, Chem. Eng. Technol. 28 (11) (2005) 1252.
[34] H.M. Hulburt, S. Katz, Chem. Eng. Sci. 19 (8) (1964) 555.
[35] J.J. van Deemter, F.J. Zuiderweg, A. Klinkenberg, Chem. Eng. Sci. 5 (1956) 271.
[36] N. Forrer, A. Butté, M. Morbidelli, J. Chromatogr. A 1214 (1–2) (2008) 59.
[37] E.J. Wilson, C. Geankoplis, Ind. Eng. Chem. Fundam. 5 (1) (1966) 9.
[38] M.E. Young, P.A. Carroad, R.L. Bell, Biotechnol. Bioeng. 22 (5) (1980) 947.
[39] M. Afzal, M. Saleem, M.T. Mahmood, J. Chem. Eng. Data 34 (3) (1989) 339.
[40] C.R. Wilke, P. Chang, AICHE J. 1 (2) (1955) 264.
[41] R. Perry, D.E. Green, Perry's Chemical Engineers' Handbook, 7th ed., McGraw-Hill, New York, NY, USA, 1997.
[42] N. Forrer, A. Butté, M. Morbidelli, J. Chromatogr. A 1214 (1–2) (2008) 71.
[43] P.V. Danckwerts, Chem. Eng. Sci. 2 (1) (1953) 1.
[44] P. DePhillips, A.M. Lenhoff, J. Chromatogr. A 933 (1–2) (2001) 57.
[45] N. Forrer, O. Kartachova, A. Butté, M. Morbidelli, Ind. Eng. Chem. Res. 47 (23) (2008) 9133.